Support Information

Ultra-Fast Polarization Modulation with High-purity Chiral Quasi-BIC Metasurfaces

Fangxing Lai [1], Yubin Fan [2], Xinbo Sha [1], Huachun Deng [1], Xiong Jiang [1], Can Huang[1,3,*], Shumin Xiao[1,3,*], Qinghai Song[1,3,*]

1, Ministry of Industry and Information Technology Key Lab of Micro-Nano Optoelectronic Information System, Guangdong Provincial Key Laboratory of Semiconductor Optoelectronic Materials and Intelligent Photonic Systems, Harbin Institute of Technology (Shenzhen), Shenzhen 518055, China

2, Department of Electrical Engineering, City University of Hong Kong, Hong Kong 999077, China

3, Heilongjiang Provincial Key Laboratory of Advanced Quantum Functional Materials and Sensor Devices, Harbin 150001, China

*Corresponding author: huangcan@hit.edu.cn; Shumin.xiao@hit.edu.cn; qinghai.song@hit.edu.cn;

Note 1. Numerical simulations

The finite element method is used for numerical simulation. Perfect matching layer is set at the top and bottom of the model to absorb the waves radiated to the outside of the simulation area. Periodic boundary conditions are set in the x and y directions. In the simulation, the resonant wavelength is around 700 nm, while the period is about 400 nm and the surrounding refractive index is 1.5. Only zero order diffracted light can be deduced from the grating formula. The plane perpendicular to the zero order is selected for calculating electric field components P_x in the x directions and P_y in the y directions. Integrating the electric field by taking the integration surface to obtain the far-field polarization component P_x and P_y[1]:

$$P_i = \frac{1}{A}\int e^{i(k_x x + k_y y)} E_i dx dy \tag{1}$$

among them, $i = x$ or y, A represents the area of a single period, k_x and k_y are Bloch wave vectors, and E_i represents the components of the electric field in the x and y directions at a certain point on the plane.

The normalized Stokes parameters are calculated by following formula to describe the polarization state, where δ represents the phase difference between P_x and P_y.

$$\begin{pmatrix} S_0 \\ S_1 \\ S_2 \\ S_3 \end{pmatrix} = \begin{pmatrix} P_x^2 + P_y^2 \\ P_x^2 - P_y^2 \\ 2P_x P_y cos\delta \\ 2P_x P_y sin\delta \end{pmatrix} \tag{2}$$

The topological charge of BIC in momentum space is calculated using the following path integration formula[2,3]:

$$q = \frac{1}{2\pi}\oint_C dk \cdot \nabla_k \varphi(k) \tag{3}$$

which describes how many times the polarization vector winds around the BIC. Here, φ represents the angle of the polarization vector, and C is a closed simple path in momentum space that goes around the BIC in the counterclockwise direction.

Figure S1 shows the angle-dependent LCP and RCP transmission in simulations after introducing refractive index changes. In the RCP transmission spectrum, there is a significant decrease in transmittance at resonance of 0 degree, which is due to the combined effect of an increase in the imaginary part of the refractive index and a change in refractive index causing the chiral point to move away from the Γ point.

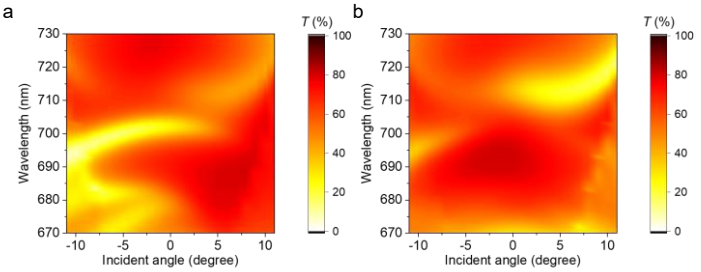

Figure S1. (a, b) The angle-dependent LCP and RCP transmission in simulations after introducing refractive index changes.

Figure S2 illustrates variations in the S_3 parameter of reflected and transmitted light following refractive index modifications. As demonstrated, the change in S_3 for transmitted light at the resonance wavelength is smaller than the corresponding change in reflected light. This difference underscores the rationale for prioritizing the characterization of S_3 variations in reflected light within the main text.

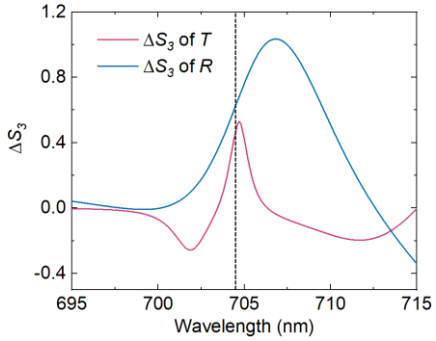

Figure S2. The variation on S_3 of reflected and transmitted light change after introducing refractive index changes. The horizontal axis of the dashed line in the figure represents the resonance wavelength of chiral quasi-BIC.

Actually, the ratio $|\Delta n/\Delta k|$ quantifies the efficiency of photoinduced refractive index modulation, where a higher value indicates stronger light-matter interaction with lower parasitic absorption. This metric, governed by free-carrier effects, is critical for achieving high-speed polarization switching in our metasurface. We calculated the Δn, Δk for α-Si is: -0.04, 0.03i for 700 nm, and -0.08, 0.14i for 1500 nm. Figure S3 illustrates the dependance of $|\Delta n/\Delta k|$ on wavelength. As wavelength grows, $|\Delta n/\Delta k|$ shows a significant downward trend, We then choose 700 nm as the operation wavelength.

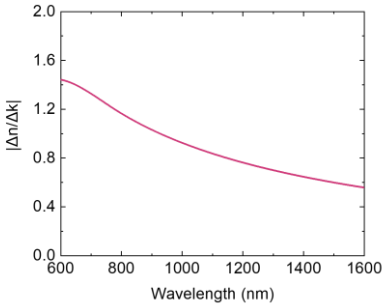

Figure S3. The $|\Delta n/\Delta k|$ curve range from 600-1600 nm.

Q-factor, ΔCD and polarization ellipticity as a function of θ and β

In the manuscript, we mentioned the parameters we choose ($\theta = 10°$, and $\beta = 23°$) is to approached the most optimize dimensions, elevated Q-values for chiral resonance coincide with enhanced CD and polarization ellipticity. Here we show the calculation details, as shown in Figure S4. Figure S4 (a-c) show the Q-factor, ΔCD and

polarization ellipticity ($\ell = \tan\left(\frac{1}{2}\arcsin\left(S_3\right)\right)$) as functions of the cooperative change of perturbations θ and β, respectively. The green pentagram markers in the figures denote the parameters presented in the main text. Notably, the slanted angle θ is constrained from 5° to 21°, as fabrication-induced inaccuracies (including angular deviations and surface roughness) would disproportionately affect chiral resonance characteristics at angles below 5°, potentially causing chiral resonance features to deviate entirely from the Γ point. We choose the parameters: θ = 10°, and β = 23° to approached the most optimize dimensions, elevated Q-values for chiral resonance coincide with enhanced CD and polarization ellipticity.

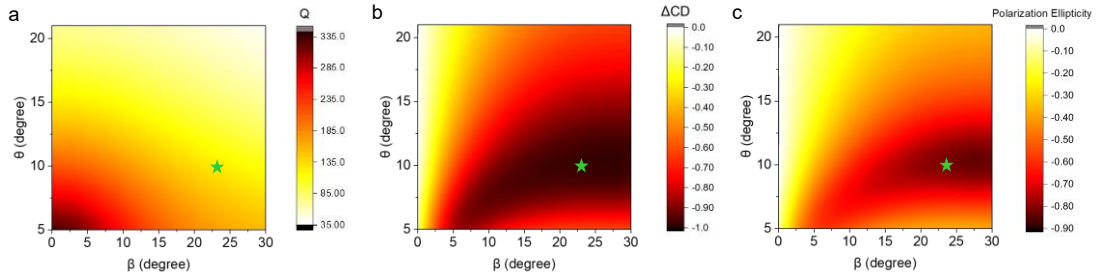

Figure S4. Simulated Q-factor, ΔCD and polarization ellipticity of the chiral BIC as functions of the cooperative change of perturbations θ and β. The green pentagrams correspond to the parameters of the chiral resonance metasurface presented in the main text.

The role played by the PMMA layer

To elucidate the role played by the PMMA layer in our design, we calculated S_3 and Q-factor of the chiral BIC as functions of the cooperative change of perturbations θ and β for the case (a) (b) with and (c) (d) without PMMA in Figure S5. The green pentagrams in the figures correspond to the parameters of the chiral resonance metasurface presented in the main text. The slanted angle θ is constrained from 5° to 21°, as fabrication-induced inaccuracies (including angular deviations and surface roughness) would disproportionately affect chiral resonance characteristics at angles below 5°, potentially causing chiral resonance features to deviate entirely from the Γ point.

As shown in panel b, the incorporation of PMMA enables a Q-factor of approximately 130 while achieving near-unity S_3 values, whereas the structure without PMMA exhibits a maximum Q-factor of 55 under identical S_3 conditions ($S_3 > 0.9$). This comparison conclusively demonstrates the Q-factor enhancement achieved with PMMA above our structure.

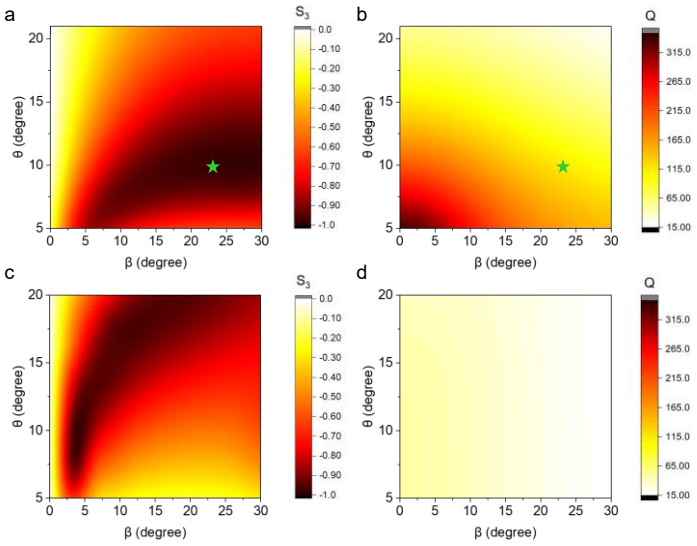

Figure S5. The calculated Stokes parameter (S_3) and Q-factor of chiral BIC as functions of the cooperative change of perturbations θ and β for the case (a)(b) with and (c)(d) without PMMA. The green pentagrams correspond to the parameters of the chiral resonance metasurface presented in the main text.

Benchmarking the system performance

The performance of the present metasurface can be evaluated quantitatively from a comparison with previously reported results from literature. Table R1 provides an overview of related studies, collecting information on Q-factor, modulation speed, energy consumption and S_3 (purity) obtained.

Ref.	Q	Modulation speed	Energy consumption (GW/cm^2)	S_3	Working wavelength	Material
This work	~118	~0.4 ps	0.088	~0.92	~700nm	α-Si
5	~56	~1 ps	0.2	~0.81	~1530nm	α-Si
6	~40	~0.27 ps	N/A	~0.78	~640nm	Au
7	~32	~0.7 ps	16	~0.71	~700nm	Au
8	~51	~3 ps	3.5	~0.68	~740nm	AlGaAs
9	~29	~0.27 ps	20	~0.74	~2.1μm	CdO
10	~12	~0.15ps	98	~0	~1.2μm	Au

Table S1: Comparison of the chiral resonance metasurface performance with relevant results from literature.

Note 2. Device fabrication

In the experiment, amorphous silicon grown by PECVD is used to fabricate chiral metasurface. The refractive index of amorphous silicon is shown in Figure S6. The refractive index is about $3.78+0.0081i$ at wavelength of 700 nm, which can support high Q-factor chiral quasi-BIC mode.

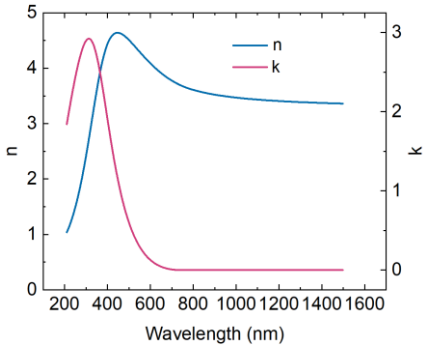

Figure S6. Complex refractive index of the initial Si film as characterized by ellipsometry

Reactive ion etching is widely used in the manufacture of nanostructure. It has been reported before that using reactive ion etching to realize the slanted etching process of silicon. In the traditional etching process, the plasma sheath is along the substrate surface, and even if the substrate is inclined, it is difficult to realize the slanted etching with accurate angle. Faraday cage can be used to realize the slanted etching of silicon [4].

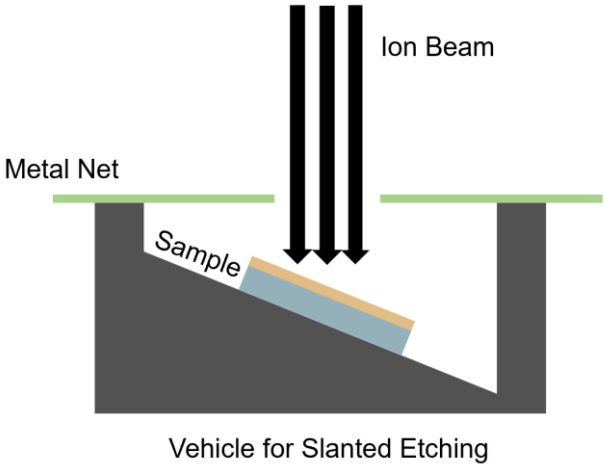

Figure S7. Schematic illustration of the slanted RIE system.

Schematic of slanted etching is shown in Figure S7. Our slanted etching gases are SF_6 and CHF_3. During slanted etching, the substrate is placed in the vehicle, and then covered with a metal net. The metal net and the vehicle form a Faraday cage with local electromagnetic shielding function to ensure that the plasma bombards the sample in a vertical downward direction, rather than perpendicular to the inclined sample, so as to ensure that the inclination angle of the structure is basically the same as that of the inclined plane of the vehicle.

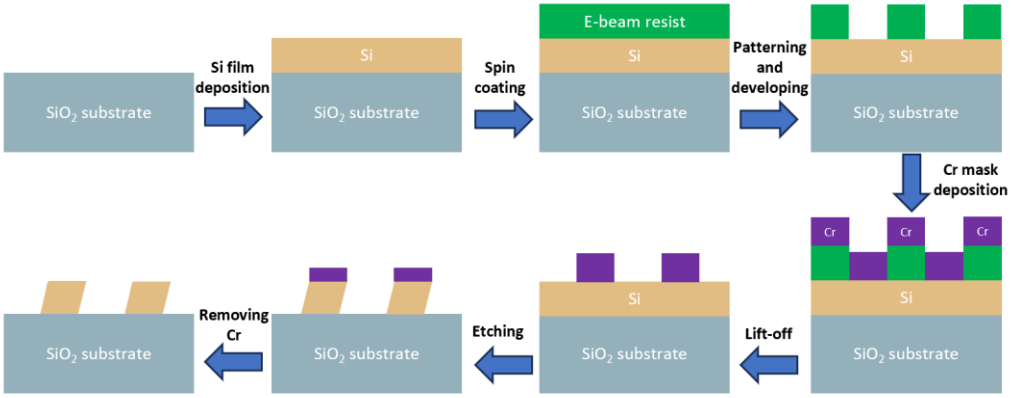

Figure S8. Flowchart for fabrication of the chiral quasi-BIC metasurface.

Chiral metasuraface is prepared by standard nanofabrication process combined with slanted etching, as shown in Figure S8. First, the 202 nm α-Si film is deposited on the SiO_2 substrate by PECVD. Secondly, an 80 nm PMMA film is spin-coated and baked at 180 °C for an hour. Next, the PMMA resist was exposed to the electron beam (Raith E-line, 30 kV) and developed in MIBK/IPA solution for 30 s at 0 °C to form the PMMA nanostructures. After the resist development, the sample is immersed in remover PG solution at room temperature for 12 hours to lift off. Then the Cr nanostructure is utilized as a mask for slanted etching. In the end, the remaining Cr film is removed by immersing the sample into the chromium etchant for 10 min.

The top view and side view SEM images of sample are shown in Figure S9, it can be seen that the sides of the silicon elliptical cylinder are parallel and smooth, with an inclination angle of about 10 ± 0.5°. The 500 nm PMMA was spin coated on the sample as a refractive index matching layer, then the chiral metasurface is obtained.

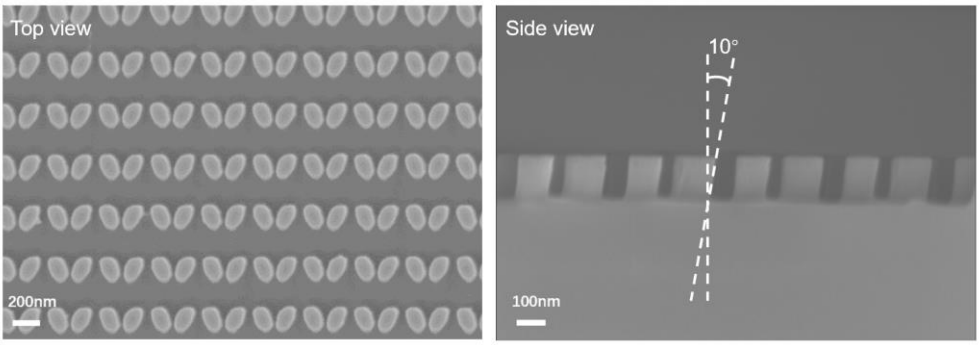

Figure S9. Top view and side view SEM image of chiral quasi-BIC metasurface

Note 3. Optical characterization

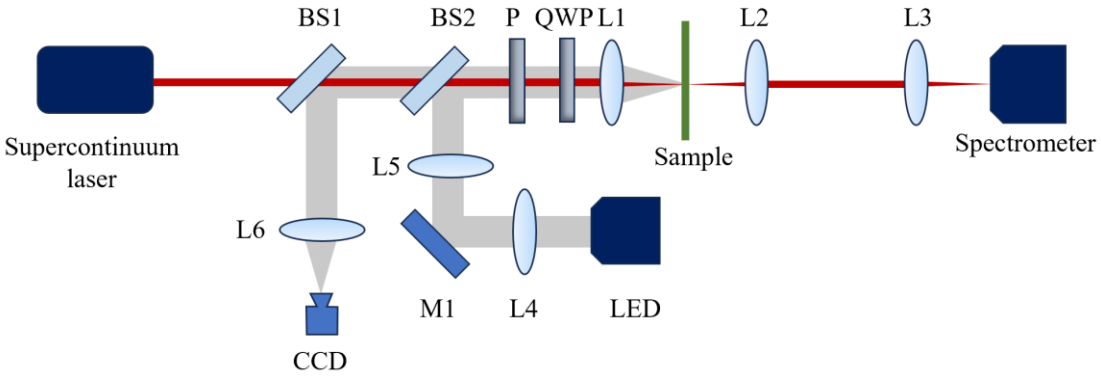

Figure S10. Experimental setup for characterizing chiroptical response of chiral QBIC metasurface under illumination by circularly polarized light. Abbreviations for optical components: BS represents beam splitter; M represents mirror; P represents polarizer; QWP represents quarter waveplate; L represents lens.

Experimental setup for characterizing chiroptical response transmission spectrum of the metasurface is shown in Figure S10. The light source is the supercontinuum light emitted by NKT super K, and its spectral range is 450-2400 nm. The supercontinuum light changes from linearly polarized light to circularly polarized light through the polarizer and quarter wave plate. The angle of the quarter wave plate can be adjusted to enable the outgoing light to LCP light or RCP light. Circularly polarized light is focused on the sample through L1, then collected by L2, and finally coupled to the spectrometer. In order to find the relative position of the sample and supercontinuum laser in the focal plane of lens, an illumination and imaging system is added to the experimental setup. In the experiment, S_3 can be calculated using the following formula.

$$S_3 = \frac{I_{RCP} - I_{LCP}}{I_{RCP} + I_{LCP}} \tag{4}$$

Experimental setup for characterizing reflected light polarization is shown in the Figure S11. The incident light passes through a polarizer and a quarter wave plate, transforming to circularly polarized light, and then focused on a chiral metasurface. The reflected light undergoes polarization detection through a quarter wave plate and a polarizer. By rotating the angle of polarizer P2, the LCP and RCP components of the reflected light can be measured.

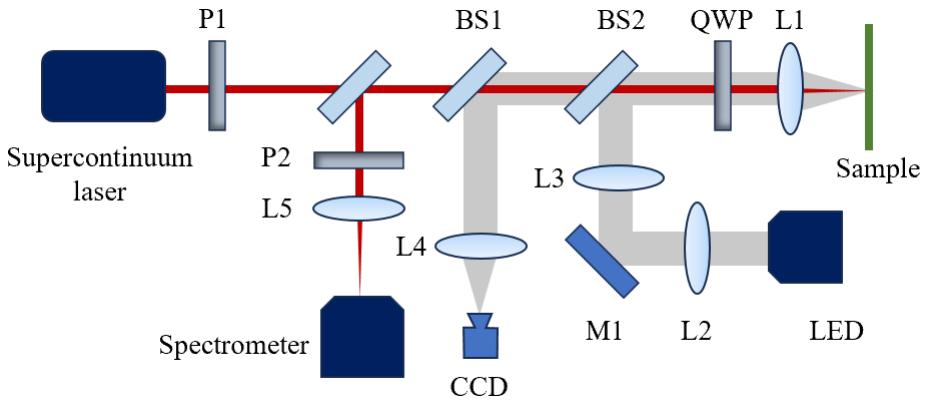

Figure S11. Experimental setup for characterizing reflected light polarization of chiral QBIC metasurface. M represents mirror; P represents polarizer; QWP represents quarter waveplate; L represents lens.

The ultrafast polarization switching effect is measured using the experimental setup depicted in Figure S12. The femtosecond light with a center wavelength of 800 nm is split into two beams. One beam is converted into 400 nm pump light through a BBO crystal. The half wave plate behind the BBO crystal can be used to change the linear polarization angle of the incident pump, ensuring the polarization state of the pumped linearly polarized light does not change after passing through the quarter wave plate.

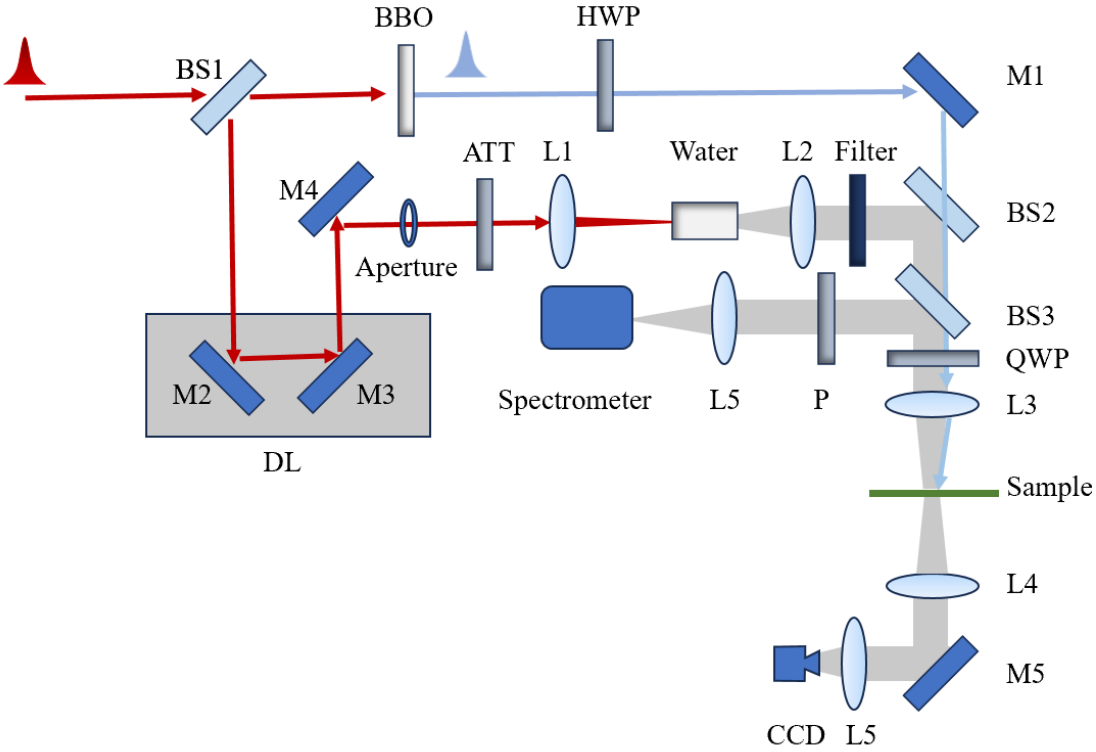

Figure S12 . The pump-probe experimental setup for characterizing ultrafast modulation on polarization of reflected light.

Another beam passes through a delay line, generating a supercontinuum light as the probe beam. By adding two lenses and a cuvette containing pure water to the path

where the probe beam located, the ultrashort pulse filament is used to produce a wide spectrum of supercontinuum light. The cuvette containing water is placed at the focus of femtosecond light. It is necessary to add an adjustable aperture and an adjustable attenuator before focusing the femtosecond laser to adjust the intensity and spot size of the femtosecond light, so that the emitted supercontinuum light is stable and relatively uniform. The generated supercontinuum light spectrum is shown in the Figure S13. During the measurement process, the supercontinuum laser and pump light are focused together on the sample. The reflected supercontinuum laser is collected into the spectrometer through a quarter wave plate and a polarizer. The LCP and RCP components of the reflected light can be measured by rotating the polarizer at different angles. By adjusting the position of the delay line, the LCP and RCP components of the reflected light with different time delays between the pump light and probe light can be measured.

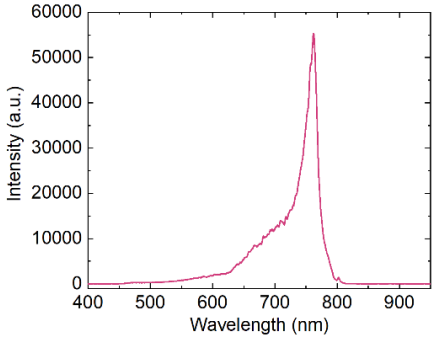

Figure S13. Spectrum of supercontinuum laser generated by focusing femtosecond pulses in water.

References

1. Chen, Y.; Deng, H.; Sha, X.; Chen, W.; Wang, R.; Chen, Y.-H.; Wu, D.; Chu, J.; Kivshar, Y. S.; Xiao, S.; Qiu, C.-W. Observation of intrinsic chiral bound states in the continuum. *Nature* **2023**, *613* (7944), 474–478.
2. Zhen, B.; Hsu, C. W.; Lu, L.; Stone, A. D.; Soljačić, M. Topological nature of optical bound states in the continuum. *Phys. Rev. Lett.* **2014**, *113* (25), 257401.
3. Liu, W.; Wang, B.; Zhang, Y.; Wang, J.; Zhao, M.; Guan, F.; Liu, X.; Shi, L.; Zi, J. Circularly polarized states spawning from bound states in the continuum. *Phys. Rev. Lett.* **2019**, *123* (11), 116104.
4. Burckel, D. B.; Finnegan, P. S.; Henry, M. D.; Resnick, P. J.; Jarecki, R. L. Oblique patterned etching of vertical silicon sidewalls. *Appl. Phys. Lett.* **2016**, *108* (14), 142103.
5. Kang, L.; Wang, C.-Y.; Guo, X.; Ni, X.; Liu, Z.; Werner, D. H. Nonlinear Chiral Meta-Mirrors: enabling technology for ultrafast switching of light polarization. *Nano Lett.* **2020**, *20* (3), 2047 − 2055.
6. Taghinejad, M.; Taghinejad, H.; Xu, Z.; Lee, K. T.; Rodrigues, S. P.; Yan, J.; Cai,

W. Ultrafast control of phase and polarization of light expedited by hot-electron transfer. *Nano Lett*. **2018**, *18* (9), 5544-5551.

7. Nicholls, L. H.; Rodríguez-Fortuño, F. J.; Nasir, M. E.; Córdova-Castro, R. M.; Olivier, N.; Wurtz, G. A.; Zayats, A. V. Ultrafast synthesis and switching of light polarization in nonlinear anisotropic metamaterials. *Nat. Photonics* **2017**, *11* (10), 628–633.
8. Crotti, G.; Akturk, M.; Schirato, A.; Vinel, V.; Trifonov, A. A.; Buchvarov, I. C.; Della Valle, G. Giant ultrafast dichroism and birefringence with active nonlocal metasurfaces. *Light Sci. Appl.* **2024**, *13* (1), 204.
9. Yang, Y.; Kelley, K.; Sachet, E.; Campione, S.; Luk, T. S.; Maria, J. P.; Brener, I. Femtosecond optical polarization switching using a cadmium oxide-based perfect absorber. *Nat. Photonics* **2017**, *11* (6), 390-395.
10. Wang, K.; Li, M.; Hsiao, H. H.; Zhang, F.; Seidel, M.; Liu, A. Y.; Ebbesen, T. High contrast, femtosecond light polarization manipulation in epsilon-near-zero material coupled to a plasmonic nanoantenna array. *ACS photonics* **2021**, *8* (9), 2791-2799.